Biomaterials
Science

rsc.li/biomaterials-science

Volume 5
Number 3
March 2017
Pages 343-602

ISSN 2047-4849

PAPER
Soo Hyun Kim et al.
Biodegradable vascular stents with high tensile and
compressive strength, a novel strategy for applying
monofilaments via solid-state drawing and shaped-annealing
processes

ROYAL SOCIETY
OF CHEMISTRY

European
Society for
Biomaterials

ROYAL SOCIETY
OF CHEMISTRY

rsc.li/biomaterials-science

SCHOLARONE™
Manuscripts

Tumor-targeted Biomimetic Nanoplatform Precisely Integrate Photodynamic Therapy and Autophagy Inhibiton for Collaborative Treatment of Oral Cancer

Hao Dai, Han Yan, Fan Dong, Ludan Zhang, Ning Du, Lisha Sun, Ningyu Li, Guohui Yu, Zeyuan Yang, Yuguang Wang* and Mingwei Huang*

Hao Dai, Han Yan and Prof. Mingwei Huang

Peking University School and Hospital of Stomatology, Beijing 100081, China.

Department of Oral and Maxillofacial Surgery, Peking University School and Hospital of Stomatology, Beijing 100081, China.

Fan Dong, Ludan Zhang, Ningyu Li, Guohui Yu, Zeyuan Yang and Prof. Yuguang Wang

Peking University School and Hospital of Stomatology, Beijing 100081, China.

National Center of Stomatology, Beijing 100081, China.

National Clinical Research Center for Oral Diseases, Beijing 100081, China.

Center of Digital Dentistry, Peking University School and Hospital of Stomatology, Beijing 100081, China

National Engineering Laboratory for Digital and Material Technology of Stomatology, Beijing 100081,China.

Biomaterials Science Accepted Manuscript

Ning Du, Lisha Sun

Central Laboratory, Peking University School and Hospital of Stomatology, Beijing

100081, China

Abstract

Oral cancer is a common malignant tumor in the maxillofacial regions. Surgical resection is the

preferred treatment, but severe functional impairment after surgery forces us to look for

noninvasive treatments. As a promising noninvasive treatment method, photodynamic therapy

(PDT) has received widespread attention in the field of cancer therapy, but the inefficient uptake

capacity of tumor cells and damage repair mechanisms limit the actual therapeutic effect. The

establishment of a targeted therapy function and autophagy inhibition strategy is considered to be

an important way to further enhance the effect of PDT. Based on this, we developed the

biomimetic nanomaterial PCN-CQ@CCM. The metal-organic framework material PCN-224 was

used as a carrier to load the autophagy inhibitor chloroquine (CQ) and coated on the surface with

isolated oral squamous cell carcinoma (OSCC) cell membranes. Due to the immune evasion and

homologous targeting ability of the biomimetic functionalized surface, PCN-CQ@CCM can

escape macrophage phagocytosis and homologously adhere to tumor cells, enhancing the retention

and uptake of nanomaterials in the tumor microenvironment. After being activated by a 660-nm

laser, the generated reactive oxygen species (ROS) triggered the apoptosis pathway as assessed by

mitochondrial damage, and the released CQ further aggravated the ROS lethal pathway by effectively inhibiting the protective autophagic flux. Therefore, PCN-CQ@CCM achieves the precise synergy of PDT and autophagy inhibition through the biomimetic homologous targeting method, and the highly effective tumor suppression effect expands a broader field of vision for the noninvasive diagnosis and treatment of oral cancer.

1. Introduction

Head and neck cancer is the seventh most common malignant tumor worldwide[1], of which oral cancer is a common subtype. Due to its high malignancy and high metastasis rates, the 5-year survival rate of patients is only approximately 60%[2]. Comprehensive treatment with surgery as the mainstay, supplemented by radiotherapy and chemotherapy, is the preferred mode of oral cancer treatment[3][4][5], but the functional tissue damage represented by the tongue will cause serious dysfunction and psychological trauma to patients[6], thus, there is an urgent need for a noninvasive, efficient, and function-preserving treatment to avoid the pain experienced by oral cancer patients. Photodynamic therapy (PDT) has entered the field of cancer therapy as a new treatment that is characterized by its noninvasiveness, time-space controllability and reproducible treatment effectiveness[7]. Oral cancer has always been regarded as a suitable type of cancer treatment for clinical PDT due to its relatively superficial location and high clinical operability[8][9][10]. The principle of PDT is to activate a photosensitizer (PS) through a light source of a certain wavelength, resulting in an explosion of lethal ROS production, including singlet oxygen[11]. These cytotoxic oxidants directly react with many biomolecules in the cell, such as proteins and DNA, and eventually lead to cell death and tissue damage[12][13]. Organic PSs often

need to rely on nanoengineering to build new delivery systems due to their hydrophobicity, but the low PS loading rate and early release phenomenon still limit their applications[14]. In the past ten years, research on metal-organic framework (MOF) photodynamic materials has shown a rapid growth trend. The unique organic light-responsive structural unit makes it a high-efficiency PS, overcoming the defects of low loading efficiency and the early release of photosensitizers, and its highly porous structure provides further drug loading performance[15]. A high PS construction ratio, low self-quenching rate, efficient ROS diffusion, high drug loading rate and flexible modifiable sites make MOF photodynamic materials a highly promising multifunctional photodynamic nanotherapy platform[16].

However, relying solely on the photodynamic action of MOF PSs still has the disadvantages of poor curative effect, a tendency for recurrence, or the need for repeated treatments for more malignant tumor types like oral cancer. Therefore, using a highly porous structure of MOFs to load drugs that have a synergistic effect with PDT will greatly improve the efficiency of combined therapy[17][18]. In recent years, protective autophagy has been considered to be an important cellular anti-injury pathway after tumor treatment, and the regulation of autophagy has been proven to be closely related to the occurrence and development of oral cancer and the outcome of treatment[19][20][21]. Therefore, the combination of autophagy inhibitors has become an effective choice for photodynamic combination treatment of oral cancer. Considering the safety and effectiveness of autophagy inhibitors, the preferred autophagy inhibitor is chloroquine (CQ) and its derivatives, which have been used clinically. By blocking the fusion and degradation of autophagosomes and lysosomes in the late stage of autophagy, cancer cells become sensitive to treatment methods, including PDT[22][23][24]. Nevertheless, passive targeting that only relies on the

enhanced permeability and retention effect (EPR) of nanomaterials is still limited by many factors,

such as the tumor microenvironment and material physical and chemical properties[25]. Autophagy

inhibition caused by CQ may not only make cancer cells and normal tissues sensitive to harmful

environments but may also accidentally damage the functions of important organs, including the

brain[26]. In addition, the systemic phototoxicity of PS is a serious side effect that has limited the

clinical use of PDT for a long time[27], therefore, it is necessary to adopt a targeting strategy to

realize the active targeted aggregation of nanodelivery platforms in oral cancer tissues and

enhance the efficacy of synergistic treatment while avoiding systemic side effects to the greatest

extent. Known targeting ligand modifications, including folic acid and aptamers, can improve

blood circulation time and achieve enhanced active tumor targeting effects, but complex synthesis

and activation of the immune system also greatly limit the general applicability of the

modification. In addition, subject to receptor density and selective recognition efficiency, ligand-

targeted nanoparticles will also experience unstable off-target effects[28][29][30]. In recent years,

nanobiomimetic technology based on cell membrane engineering has been greatly advanced.

Cancer cell membranes (CCMs) can achieve immune escape and homotype targeting of materials

due to their unique surface antigens when applied to nanoparticles[31][32][33]. This simple and

feasible targeted modification technology can enhance the enrichment of materials in tumor

tissues, reduce the distribution of other important organs and tissues, and realize the active

targeted therapy of the multifunctional nanoplatform.

Based on this, we developed the autophagy-inhibiting photodynamic nanoplatform PCN-

CQ@CCM coated with an oral cancer cell membrane and, for the first time, realized the precise

synergistic antitumor effect of PDT and autophagy inhibition guided by biomimetic membrane

technology. After the nanoparticles enter the blood circulation, because of the camouflage effect of the oral cancer cell membrane coated on the surface, they are able to escape the immune system and are capable of homologous targeting. Efficient accumulation avoids possible systemic side effects and enhances ROS damage and the inhibition of protective autophagy, ultimately effectively inhibiting the growth of oral cancer (Fig. 1). This noninvasive, targeted, spatiotemporally controllable treatment mode will maximize the preservation of normal tissues and organs involved in the tumor and will greatly enhance the preservation and functional maintenance of the oral and jaw systems affected by oral cancer. This methodology is expected to achieve precise, noninvasive, and personalized nanodiagnosis and treatment of oral cancer in the future.
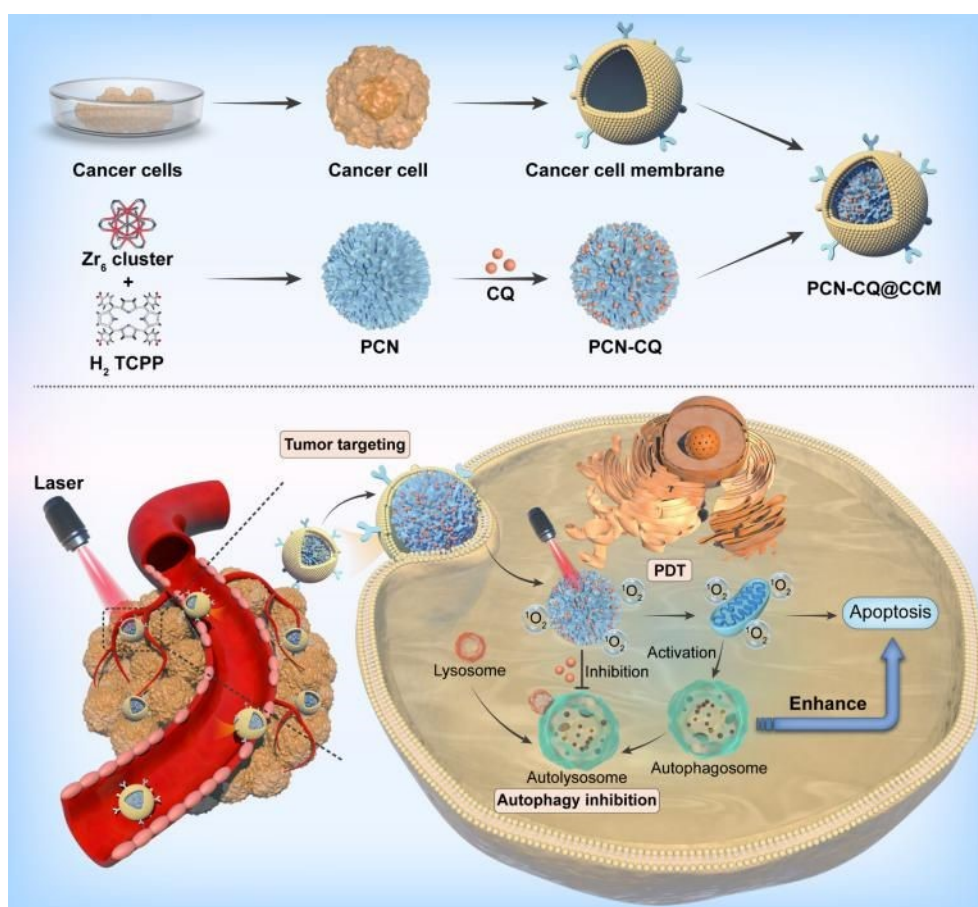

Fig. 1. Synthesis of PCN-CQ@CCM and its targeted and cooperative antitumor mechanism.

2. Experiment Section

2.1 Materials

ZrOCl$_2$·8H$_2$O, benzoic acid and silicone oil were purchased from Sigma–Aldrich. TCPP was purchased from Energy Chemical. DMF was purchased from MACKLIN. Chloroquine and JC-1 were purchased from Solarbio. DCFH-DA was purchased from APE Bio. Annexin V-FITC/PI was purchased from Beyotime Biotechnology. CCK-8 was purchased from DOJINDO. Antibodies for western blotting were purchased from Abcam. All other reagents and consumables for cell experiments were purchased from Corning. Cells were from the Central Laboratory of Peking University Stomatological Hospital, and experimental animals were purchased from Charles River. The flow cytometer was an EPICS XL of Beckman Coulter, the gel imaging system was a FUSION FX-5 from VILBER, the multi-mode microplate inspection system was an Enspire from PerkinElmer, the CLSM was an LMS710 from Zeiss, the fluorescence microscope was a BX53 from Olympus, and the SEM was an SU8010 from Hitachi.

2.2 Synthesis of PCN, PCN-CQ and PCN-CQ@CCM

We synthesized PCN-224 according to the method shown in the report[34]. In brief, benzoic acid, ZrOCl$_2$·8H$_2$O and tetrakis TCPP were dissolved in DMF and stirred at 90 °C for 5 h. Then, the mixture was centrifuged at 15,000 rpm for 30 min and washed with DMF 3 times. The prepared PCN-224 was freeze-dried and stored at 4°C. The standard curve of TCPP was made from the characteristic peak at 415nm, and PCN-224 uses this standard curve to determine the concentration of nanomaterials with the effective concentration of TCPP. We made a CQ standard

curve based on the characteristic UV-visible absorption peaks of CQ at 228nm, dispersed PCN-

224 in ddH$_2$O and added CQ of different qualities. Then, then we shook the mixture at room

temperature overnight, centrifuged it at 15,000 rpm for 15 min and discarded the supernatant to

obtain PCN-CQ. The measurement of the CQ content in the supernatant indicated the drug loading

and drug encapsulation rates under different dosage ratios (CQ : PCN = 0.25, 0.5, 0.75, 1). We

cultivated the human oral cell carcinoma Cal-27 cell line in logarithmic growth phase and used a

membrane protein extraction kit to obtain free Cal-27 cell membrane fragments. The obtained

mixture was centrifuged (4 °C, 800 x g, 10 min), and the supernatant was centrifuged (14,000 x g,

30 min). Finally, the Cal-27 cell membrane was obtained by lyophilization. Then, 0.5 mL of PCN-

224 (2 mg/mL) and 0.5 mL of Cal-27 cell membranes (2 mg/mL) were added to the mixture.

Then, we coextruded Cal-27 cell membranes and PCN-CQ with an Avanti mini extruder using a

polycarbonate porous membrane (400 nm).

2.3 Characterization of the physical and chemical properties of PCN, PCN-CQ, and PCN-CQ@CCM

The morphologies of PCN, PCN-CQ, and PCN-CQ@CCM were detected and analyzed by

scanning electron microscopy (SEM) and transmission electron microscopy (TEM). TEM

elemental mapping of PCN-CQ@CCM was detected by TEM. The zeta potential and

hydrodynamic diameter of PCN, PCN-CQ, and PCN-CQ@CCM were detected by the dynamic

light scattering method. The surface proteins of PCN, PCN-CQ, and PCN-CQ@CCM were

detected by agarose gel electrophoresis. The uv-vis spectra of CQ, PCN, PCN-CQ, and PCN-CQ@CCM and the fluorescence spectra of PCN, PCN-CQ, and PCN-CQ@CCM were obtained

by multi-mode microplate inspection system.

2.4 ROS generation and CQ release of PCN-CQ@CCM

ROS generation in PCN-CQ@CCM at different time points after laser irradiation was detected by the ROS probes DCFH, which were obtained from DCFH-DA under alkaline conditions, DCFH-DA was dissolved in an aqueous solution of sodium hydroxide, and after standing at room temperature for 20 minutes, it is adjusted back to a neutral solution with PBS solution. The drug release behavior of PCN-CQ@CCM was tested by the dialysis bag method. A dialysis bag containing 2 ml and 1 mg/ml PCN-CQ@CCM was supplemented with 10 ml of HEPES solution (pH=7.5) or acetic acid hydrochloric acid buffer (pH=5.5/6.5) for dialysis at 200 rpm and 37℃. In different time intervals, 1 ml of buffer was used for uv-vis analysis, and 1 ml of fresh buffer was added to the dialysis medium. The cumulative release of CQ at different time points was quantified according to a standard curve.

2.5 Cell culture

Cal-27, HeLa, MDA-MB-231, B16, RAW264.7 and HaCaT cells were cultured at 37 °C and 5% CO_2 using 10% FBS, 1% penicillin & streptomycin and DMEM.

2.6 Cellular uptake of PCN, PCN-CQ, PCN-CQ@CCM

For the confocal laser scanning microscopy (CLSM) imaging of Cal-27 cellular uptake, Cal-27 cells in the logarithmic growth phase were inoculated into a CLSM dish with an inoculation density of approximately $2*10^5$/dish. After 24 hours of incubation in the incubator, each

Biomaterials Science

experimental group was replaced with PBS, PCN, PCN-CQ, or PCN-CQ@CCM, in which the effective concentration of TCPP was 3 μM. After 4 hours, the cells were washed 3 times with fresh PBS, and fresh serum-containing medium was replaced. After adding DAPI dye (10 μM) for approximately 0.5 hours, the intracellular fluorescence of each experimental group was observed with CLSM. For CLSM imaging of other tumor cellular uptake, Cal-27, HeLa, MDA-MB-231, and B16 cells in the logarithmic growth phase were seeded into CLSM dishes with a seeding density of approximately $2*10^5$/dish. After 24 hours of incubation in the incubator, each experimental group was replaced with PBS, PCN, and PCN-CQ, PCN-CQ@CCM for processing, and follow-up operations were performed as before. For CLSM imaging of macrophage cellular uptake, RAW264.7 cells in the logarithmic growth phase were seeded into a CLSM dish with a seeding density of approximately $2*10^5$/dish. After 24 hours of incubation in the incubator, each experimental group was replaced with PBS, PCN, PCN-CQ, and PCN-CQ@CCM, and follow-up operations were performed as before. For the flow cytometry (FCM) analysis of Cal-27 cellular uptake, Cal-27 cells in the logarithmic growth phase were inoculated into a 6-well plate with an inoculation density of approximately $4*10^5$/well. After 24 hours of incubation in the incubator, each experimental group was replaced with PBS, PCN, PCN-CQ, and PCN-CQ@CCM, where the effective concentration of TCPP was 3 μM. After 4 hours, the cells were washed 3 times with fresh PBS solution, each group of cells was digested with trypsin without EDTA, the supernatant was discarded by centrifugation at 1000 rpm for 5 min, and the cells were resuspended in PBS. Then, the samples of each group were tested by flow cytometry.

2.7 Intracellular ROS generation of PCN, PCN-CQ, PCN-CQ@CCM

For CLSM imaging of cellular ROS, Cal-27 cells in the logarithmic growth phase were inoculated into a CLSM dish with an inoculation density of approximately $4*10^5$/dish. After 24 hours of incubation in the incubator, each experimental group was replaced with PBS, PCN, and PCN-CQ, PCN-CQ@CCM for processing, in which the effective concentration of TCPP was 3 μM. After 4 hours, the cells were washed 3 times with fresh PBS and were supplemented with fresh serum-containing medium with DCFH-DA (10uM). In each experimental group, intracellular fluorescence was detected by CLSM immediately after treatment without or with a laser (660 nm, 100 mW/cm^2, 5 min). The same group culture and incubation conditions were partly adopted by FCM. Cells in each group were digested with trypsin without EDTA, centrifuged at 1000 rpm for 5 min to discard the supernatant, resuspended in PBS, and irradiated with 660nm, 100mW/cm^2, 5min or not , finally detected by flow cytometry.

2.8 Mitochondrial depolarization caused by PCN, PCN-CQ, PCN-CQ@CCM

For CLSM imaging of cellular mitochondrial depolarization, Cal-27 cells in the logarithmic growth phase were inoculated into CLSM dishes with an inoculation density of approximately $4*10^5$/dish. After 24 hours of incubation in the incubator, each experimental group was replaced with PBS, PCN, PCN-CQ, and PCN-CQ@CCM for processing, in which the effective concentration of TCPP was 3 μM. After 4 hours, the cells were washed 3 times with fresh PBS, fresh serum-containing medium was added, and each experimental group received no laser or laser (660 nm, 100 mW/cm^2, 5 min). Then, JC-1 dye (10 μM) was added for approximately 0.5 h, and the cells were washed 3 times with fresh PBS. All experimental groups were detected by CLSM immediately. For FCM analysis of cellular mitochondrial depolarization, Cal-27 cells in the

logarithmic growth phase were inoculated into a 6-well plate so that the inoculation density was

approximately $4*10^5$/dish. After 24 hours of incubation in the incubator, each experimental group

was replaced with PBS, PCN, PCN-CQ, and PCN-CQ@CCM, in which the effective

concentration of TCPP was 3 μM. After 4 hours, the cells were washed 3 times with fresh PBS.

After treatment with no laser or laser (660 nm, 100 mW/cm^2, 5 min), each experimental group was

digested with trypsin without EDTA, centrifuged at 1000 rpm for 5 min to discard the supernatant,

resuspended in PBS solution, and JC-1 dye was added (10 μM). Then, flow cytometry was

performed for detection after 0.5 h.

2.9 Apoptosis caused by PCN, PCN-CQ, and PCN-CQ@CCM

For the CLSM imaging of live or dead cells, Cal-27 cells in the logarithmic growth phase were

inoculated into CLSM dishes with an inoculation density of approximately $4*10^5$/dish. After 24

hours of incubation in the incubator, each experimental group was replaced with PBS, PCN, and

PCN-CQ, and PCN-CQ@CCM for processing, in which the effective concentration of TCPP was

3 μM. After 4 hours, the cells were washed 3 times with fresh PBS, and fresh serum-containing

medium was added. After treatment with no laser or laser (660 nm, 100 mW/cm^2, 5 min), Annexin

V-FITC/PI dye (10 μM) was added to each experimental group, and after 0.5 h, intracellular

fluorescence was detected by CLSM. For the FCM experiment of apoptosis/necrosis, after treating

cells in the same way as above, cells in each group were digested with trypsin without EDTA,

centrifuged at 1000 rpm for 5 min to discard the supernatant, resuspended in PBS, supplemented

with Annexin V-FITC/PI dye (10 μM) for approximately 0.5 h, and then detected by flow

cytometry. For the CCK-8 method to detect live cells, Cal-27 cells in the logarithmic growth

phase were inoculated into 96-well plates with a n inoculation density of approximately

$5*10^3$/well. After 24 hours of incubation in the incubator, each experimental group was replaced

with PBS, PCN, PCN-CQ, and PCN-CQ@CCM, where the effective concentrations of TCPP

were 0.5, 1, 1.5, 2, 2.5, and 3 μM. After 4 hours, the cells were washed 3 times with fresh PBS,

and fresh serum-containing medium was added. Each experimental group was treated with no

laser or laser (660 nm, 100 mW/cm^2, 5 min) and then placed in the incubator to continue

incubating for 24 h. Then, fresh medium containing 10% CCK-8 detection agent was added, and

after approximately 2 h, the OD value at 450 nm was measured with a microplate reader. After the

HaCaT cells were incubated with the materials, the cell activity was detected by CCK-8 under the

condition of no irradiation, and the experimental procedure was the same as above.

2.10 PCN-CQ@CCM inhibits protective autophagy

For the western blot analysis to detect LC3- I / II, Cal-27 cells in the logarithmic growth phase

were inoculated into a 6-well plate, with an inoculation density of approximately $4*10^5$/dish. After

24 hours of incubation in the incubator, each experimental group was replaced with PBS, PCN,

PCN-CQ, and PCN-CQ@CCM for processing, in which the effective concentration of TCPP was

3 μM. After 4 hours, the cells were washed 3 times with fresh PBS, and 100 μl of RIPA solution

was added to each well. After 0.5 h of incubation in an ice bath, the cells of the experimental

group were scraped with a cell scraper to collect them. Then, the samples were lysed using an

ultrasonic disruptor and centrifuged at 15,000 rpm for 5 min, and the supernatant was taken to

obtain a protein sample. A preprepared 12% concentration gel and an 8% separating gel were used

for vertical electrophoresis and transfer to a membrane at room temperature. The LC3- I / II

primary antibody was diluted 1:2000 and incubated overnight at 4 °C, and the secondary antibody

was diluted 1:5000 and was incubated for 2 hours. Following incubation, the membrane was

developed on a machine. For Bio-TEM to detect cellular autophagy inhibition, Cal-27 cells in the

logarithmic growth phase were inoculated into a 6-well plate with an inoculation density of

approximately $4*10^5$/dish. After 24 hours of incubation in the incubator, each experimental group

was replaced with PBS, PCN, PCN-CQ, and PCN-CQ@CCM for processing, in which the

effective concentration of TCPP was 3 μM. After 4 hours, the cells were washed 3 times in fresh

PBS. After treatment with a laser (660 nm, 100 mW/cm^2, 5 min), each experimental group was

digested with trypsin without EDTA, centrifuged at 1000 rpm for 5 min to discard the supernatant,

resuspended and fixed with 2.5% glutaraldehyde, and then observed by transmission electron

microscopy.

2.11 Animal fluorescence imaging of PCN, PCN-CQ, and PCN-CQ@CCM

The back tumor-bearing nude mouse model of oral squamous cell carcinoma Cal-27 was

constructed by subcutaneous injection of $2*10^6$ Cal-27 cells. When the tumors grew to

approximately 100 mm^3 (long diameter * short diameter * short diameter * 1/2), PCN, PCN-CQ,

and PCN-CQ@CCM saline solutions (200 μl, 1 mg/ml) were injected through the tail vein, and

the fluorescence distribution in the body was detected using an animal fluorescence imaging

instrument at 1 h, 12 h, 24 h, 48 h, 72 h and 96 h after injection. After 96 hours, each group of

nude mice was killed, and tumors and important organs were collected and detected using an

animal fluorescence imaging instrument.

2.12 Antitumor effects of PCN, PCN-CQ, and PCN-CQ@CCM in vivo

A nude mouse model of Cal-27 oral squamous cell carcinoma with tumors on the back was constructed by subcutaneous injection of $2*10^6$ Cal-27 cells. After the tumors grew to approximately 100 mm^3 (long diameter * short diameter * short diameter * 1/2), the animals were randomly divided into 7 groups, with 5 animals in each group. Nude mice in each experimental group were given tail vein administration at a dose of 1 mg/ml and 200 μl of nanomaterials for each injection. After being protected from light for 24 hours, the tumor-bearing mice in each experimental group were treated with no laser or laser (660 nm, 100 mW/cm^2, 5 min). Subsequently, tumor growth was observed periodically, and the tumor volume and weight of the nude mice were recorded every 3 days. All experimental animals were sacrificed after 21 days. The isolated tumors of each experimental group were collected, photographed, and weighed; tissue sections were produced; and H&E staining was performed. Important organs were sectioned, H&E stained and observed by a fluorescence microscope.

2.13 Hemolysis analysis of PCN-CQ@CCM

The hemolysis test was used to evaluate the in vitro cytotoxicity of PCN-CQ@CCM. 4 mL rabbit heart blood was collected by EDTA anticoagulant blood vessel. The red blood cells were collected by centrifugation and washed twice with PBS solution. 0.5ml of red blood cell PBS solution was mixed with PCN-CQ@CCM PBS solution (3, 10, 50 and 100 μM). PBS and water were used as negative control and positive control, respectively. All samples were gently mixed and stored at room temperature for 3 h. The absorbance of the supernatant after centrifugation was measured at a wavelength of 570 nm. Hemolysis rate = (sample absorbance − negative control absorbance) /

(positive control − negative control absorbance)×100.

3. Results and Discussion

3.1 Material characterization of PCN-CQ@CCM

To prepare the biomimetic nanomaterial PCN-CQ@CCM, we prepared PCN-224 nanoparticles with a uniform morphology according to previous research methods and then successfully loaded the autophagy inhibitor chloroquine CQ with excellent pore-loading characteristics. We successfully obtained free cancer cell membranes from the Cal-27 human oral squamous cell carcinoma line cultured in vitro by the membrane protein extraction method and further synthesized the biomimetic nanomaterial PCN-CQ@CCM by coextruding PCN-CQ and free cancer cell membranes. According to the SEM results of PCN-CQ@CCM (Fig. 2a), PCN (Fig. S1a) and PCN-CQ (Fig. S1b), we finally synthesized nanoparticles with uniform size and morphology. The TEM results further showed that the PCN-CQ@CCM we synthesized had a shell of approximately 10 nm, comparable to PCN-CQ, suggesting that the cancer cell membrane was successfully coated on the surface of PCN-CQ (Fig. 2b). TEM elemental mapping images showed that PCN-CQ@CCM had carbon, zirconium, and phosphorus elements (Fig. 2c), and the identification of phosphorus elements in particular was proven to contain cell membrane components, which supported the coating of cancer cell membranes. According to the results of hydrodynamic diameter detection, PCN was approximately 100 nm, PCN-CQ was approximately 125 nm, and PCN-CQ@CCM was approximately 150 nm (Fig. 2d). Zeta potential test results showed that PCN and PCN-CQ materials had obvious positive surface charge (+30 mv), while PCN-CQ@CCM had obvious negative surface charge (-37 mv) (Fig. 2e). To our best knowledge,

free cell membrane proteins usually exhibit a negative charge in the liquid phase, therefore, the
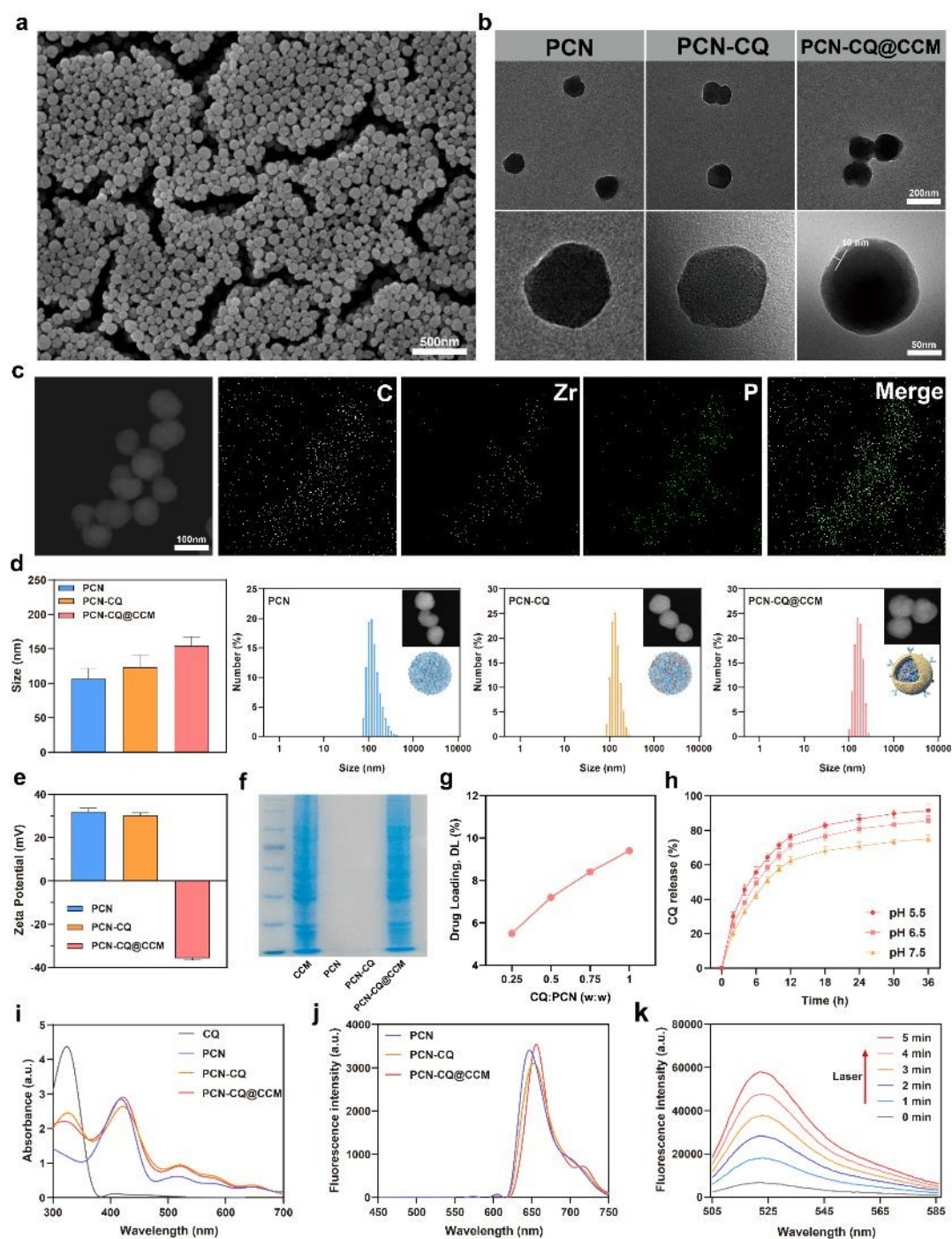

Fig. 2 Characterization of the physical, chemical and optical properties of PCN-CQ@CCM. (a) SEM of PCN-CQ-

CCM, scale bar = 500 nm. (b) TEM of PCN, PCN-CQ, and PCN-CQ@CCM; scale bar = 200 nm, scale bar = 50

nm. (c) TEM elemental mapping images of PCN-CQ@CCM. (d) DLS of PCN, PCN-CQ, and PCN-CQ@CCM,

scale bar = 100 nm. (e) Zeta potentials of PCN, PCN-CQ, and PCN-CQ@CCM. (f) SDS–PAGE protein analysis

of CCM, PCN, PCN-CQ, and PCN-CQ@CCM. (g) The drug loading rate of PCN to CQ according to different

feeding ratios. (h) The cumulative drug release ratio of PCN-CQ under different pH conditions. (i) UV-vis spectra

of CQ, PCN, PCN-CQ, and PCN-CQ@CCM. (j) Fluorescence spectra of PCN, PCN-CQ, and PCN-CQ@CCM.

(k) ROS generation of PCN-CQ@CCM (660 nm, 100 mW/cm^2, 5min).

zeta potential results further supported the success of cancer cell membrane coating on the surface

of PCN-CQ. An agarose gel electrophoresis experiment was performed to further verify the

success of the cancer cell membrane coating. As shown in the results, only the PCN-CQ@CCM

lane showed Coomassie brilliant blue staining, similar to free CCM, which proved that the PCN-

CQ@CCM group contained membrane proteins, indicating that the cancer cell membrane was

successfully coated on the surface of PCN-CQ (Fig. 2f). According to the characteristic absorption

peak of CQ at a wavelength of 228 nm (Fig. S4), we used UV-Vis to detect the drug loading

performance of PCN-224 as a carrier for the autophagy inhibitor CQ, and the results showed that

as the feeding ratio of CQ:PCN increased, an increased drug loading rate and a decreased drug

encapsulation efficiency were obtained (Fig. 2g, Fig. S3). It is worth noting that when the

CQ:PCN ratio was approximately 1:1, a drug loading efficiency of approximately 10% could be

obtained; as a result, the following material preparations were synthesized according to the feed

ratio. Subsequently, the drug release characteristics of CQ in vitro were also detected by the UV-

Vis method, and we found that PCN-CQ had a faster and higher drug release rate in a slightly

acidic environment (Fig. 2h). This feature will help the nanodelivery system have a certain

controlled release effect in the slightly acidic tumor microenvironment and improve the

bioavailability and biosafety of the drug. In contrast, the CQ release rate of PCN-CQ@CCM

under the same conditions was greatly reduced (Fig. S5a). This is because the biomimetic cell

membrane has an encapsulating effect on loading drugs, which is beneficial to avoid early release

of drugs during circulation in the body. In addition, PCN-CQ@CCM after irradiation had a greatly

enhanced drug release rate (Fig. S5b). This is due to the degradation of the bionic cell membrane

induced by ROS[35]. This feature determines the excellent spatiotemporal controllability and

biological safety of PCN-CQ@CCM. The visible light absorption and fluorescence spectra

corresponding to the materials are shown in (Fig. 2i, j). CQ was successfully loaded on PCN

according to the characteristic absorption peak of CQ at 342 nm, and the use of DCFH-DA as an

ROS probe to detect the ROS generation of PCN-CQ@CCM in vitro is shown in Fig 2k. As the

irradiation time increased, the fluorescence intensity of the test sample at 525 nm also increased.

The fluorescence intensities of ROS caused by PCN and PCN-CQ under the same conditions were

consistent with that of PCN-CQ@CCM, which proved that loading drugs or encapsulating cell

membranes will not reduce ROS generation (Fig. S6).

3.2 Cellular uptake of PCN-CQ@CCM

Based on the bionic performance characteristics of PCN-CQ@CCM, we prioritized the

homologous targeting of PCN-CQ@CCM to Cal-27 cancer cells. According to the fluorescence

characteristics of the PCN carrier itself, we used CLSM to detect Cal-27 cells after material

uptake. The fluorescence intensity inside, as shown in the results, revealed that the PCN-

CQ@CCM group showed significantly enhanced fluorescence intensity compared to the PCN and

PCN-CQ groups (Fig. 3b). This suggested that the PCN-CQ@CCM group had more

nanomaterials taken up into Cal-27 cells than the other experimental groups, which proved that the

Biomaterials Science

coating of the homogenous cancer cell membrane could enhance the tumor uptake performance of

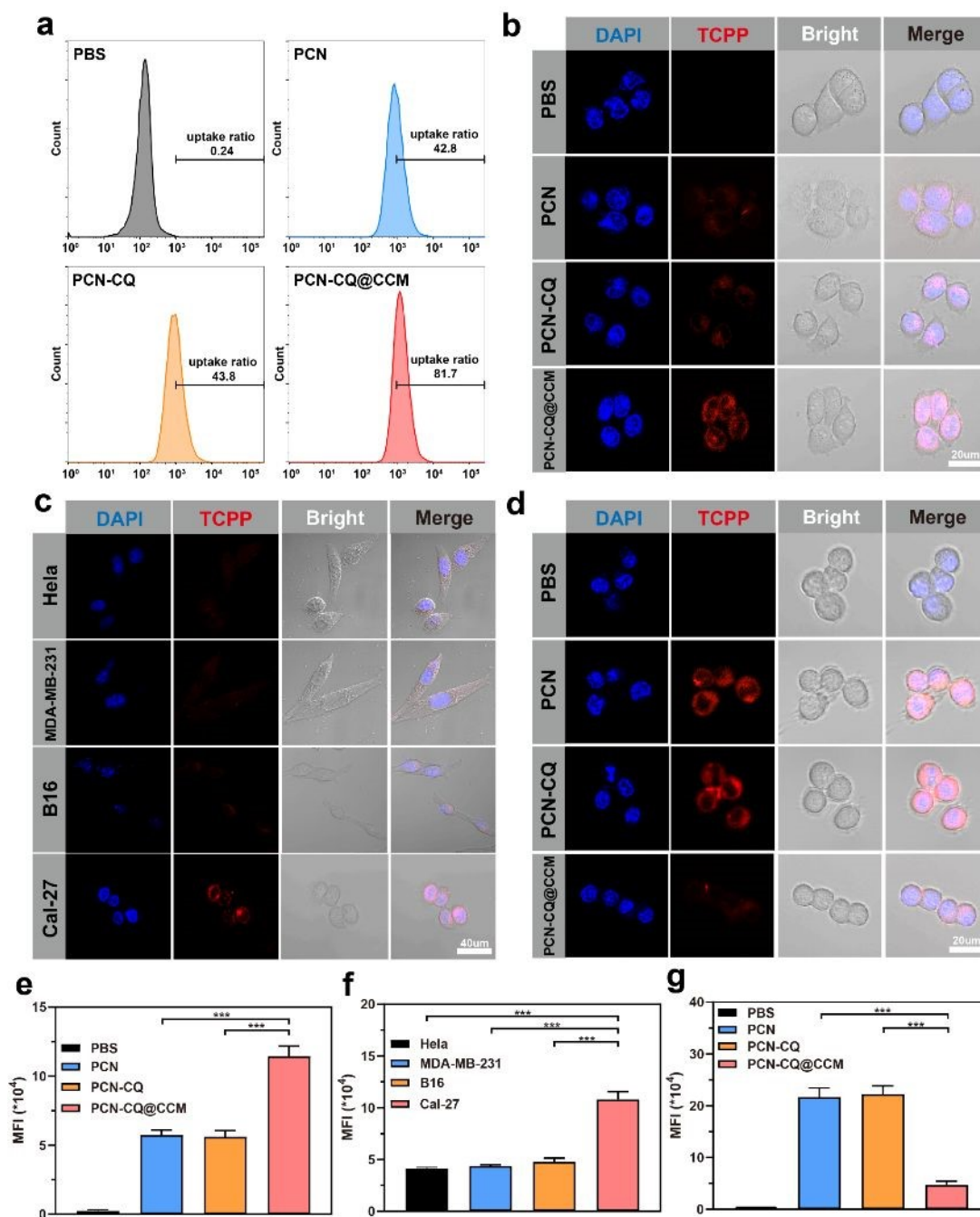nanomaterials. Similarly,

Fig. 3 Cellular uptake of PCN-CQ@CCM. (a) FCM to detect the proportions of PCN, PCN-CQ, and PCN-

CQ@CCM taken up by Cal-27 cells. (b) CLSM images of Cal-27 cells taking up PCN, PCN-CQ, and PCN-

CQ@CCM; scale bar = 20 μm. (c) CLSM images of HeLa, MDA-MB-231, B16 and Cal-27 cells taking up PCN-

CQ@CCM; scale bar = 40 μm. (d) CLSM images of RAW264.7 cells taking up PCN, PCN-CQ, and PCN-

Biomaterials Science Accepted Manuscript

CQ@CCM; scale bar = 20 μm. (e, f, g) Quantitative analysis of fluorescence intensity determined by ZEN Blue

software, n = 3, *** p < 0.001.

the uptake of Cal-27 cells for different groups of materials was evaluated by FCM. The results

showed that the tumor uptake rate of PCN-CQ@CCM was 81.7%, which was significantly higher

than those of PCN (42.8%) and PCN-CQ (43.8%), proving that biomimetic membrane technology

improved the cell uptake rate of nanomaterials (Fig. 3a). To further consider whether this

improved material uptake capacity is specific, we used HeLa, MDA-MB-231 and B16 cells to

compare the uptake capacity of Cal-27 cells for PCN-CQ@CCM. The results of CLSM showed

that the uptake capacity of the other three tumor cells for PCN-CQ@CCM was not as good as that

of Cal-27 cells (Fig. 3c), indicating that this enhanced uptake performance derived from specific

cancer cell membranes has homology and specificity. In addition, according to reports, the cancer

cell membrane surface antigen of the biomimetic membrane technology can confer significant

immune escape performance to nanomaterials; therefore, we used RAW264.7 cells to evaluate the

immune escape performance of PCN-CQ@CCM, and the results of CLSM showed that the

fluorescence intensity of the PCN-CQ@CCM group was significantly weaker than those of the

PCN and PCN-CQ groups (Fig. 3d). This indicated that the nanomaterials coated with cancer cell

membranes had the ability to avoid phagocytosis by mononuclear macrophages, which will help

extend the blood circulation time and increase the bioavailability of the material when used in

vivo. The fluorescence intensity of all CLSM images was semiquantitatively analyzed (Fig. 3e, f,

g). Obviously, PCN-CQ@CCM derived from oral squamous cell carcinoma membrane

modification only had an enhanced uptake ability for homologous cancer cells but had a repelling

effect on tumor cells and monocyte macrophages from other sources.

3.3 PCN-CQ@CCM triggers cell apoptosis

Based on the excellent material properties and bionic performance of PCN-CQ@CCM, we further evaluated the antitumor performance of PCN-CQ@CCM in vitro. DCFH-DA was used as a fluorescent probe to detect the generation of intracellular ROS. Each experimental group received nanomaterial incubation and DCFH-DA staining. After not receiving or receiving laser, CLSM was performed to observe intracellular ROS generation. As shown in the results, only the PCN+L, PCN-CQ+L and PCN-CQ@CCM+L groups showed green fluorescence, as indicated by the presence of ROS, among them, the PCN-CQ@CCM+L group had significantly enhanced fluorescence intensity compared with the other two groups (Fig. 4a). Similarly, we used FCM to verify the intracellular ROS production, and obtained similar results between groups (Fig. S7). We believe that the Cal-27 cells in the PCN-CQ@CCM+L group under the same incubation conditions had taken up more PCN vectors with photoinduced ROS effects due to the action of the homologous cancer cell membrane and therefore exhibited enhanced green fluorescence. Mitochondrial damage caused by ROS is considered to be an important antitumor mechanism of PDT. Therefore, we used the mitochondrial membrane potential probe JC-1 to evaluate the mitochondrial damage ability of PCN-CQ@CCM. Each experimental group received nanomaterial coincubation and JC-1 staining, and CLSM was used to observe the depolarization of mitochondrial membrane potential after not receiving or receiving laser. The PBS, PBS+L, PCN, PCN-CQ and PCN-CQ@CCM groups all showed red fluorescence with normal mitochondrial membrane potential, while the PCN+L, PCN-CQ+L and PCN-CQ@CCM+L

groups showed green fluorescence with depolarization of the mitochondrial membrane potential,

which proved that the production of ROS led to the depolarization of mitochondria in the cell (Fig.

3d). It is worth mentioning that the PCN-CQ@CCM+L group showed a higher green fluorescence
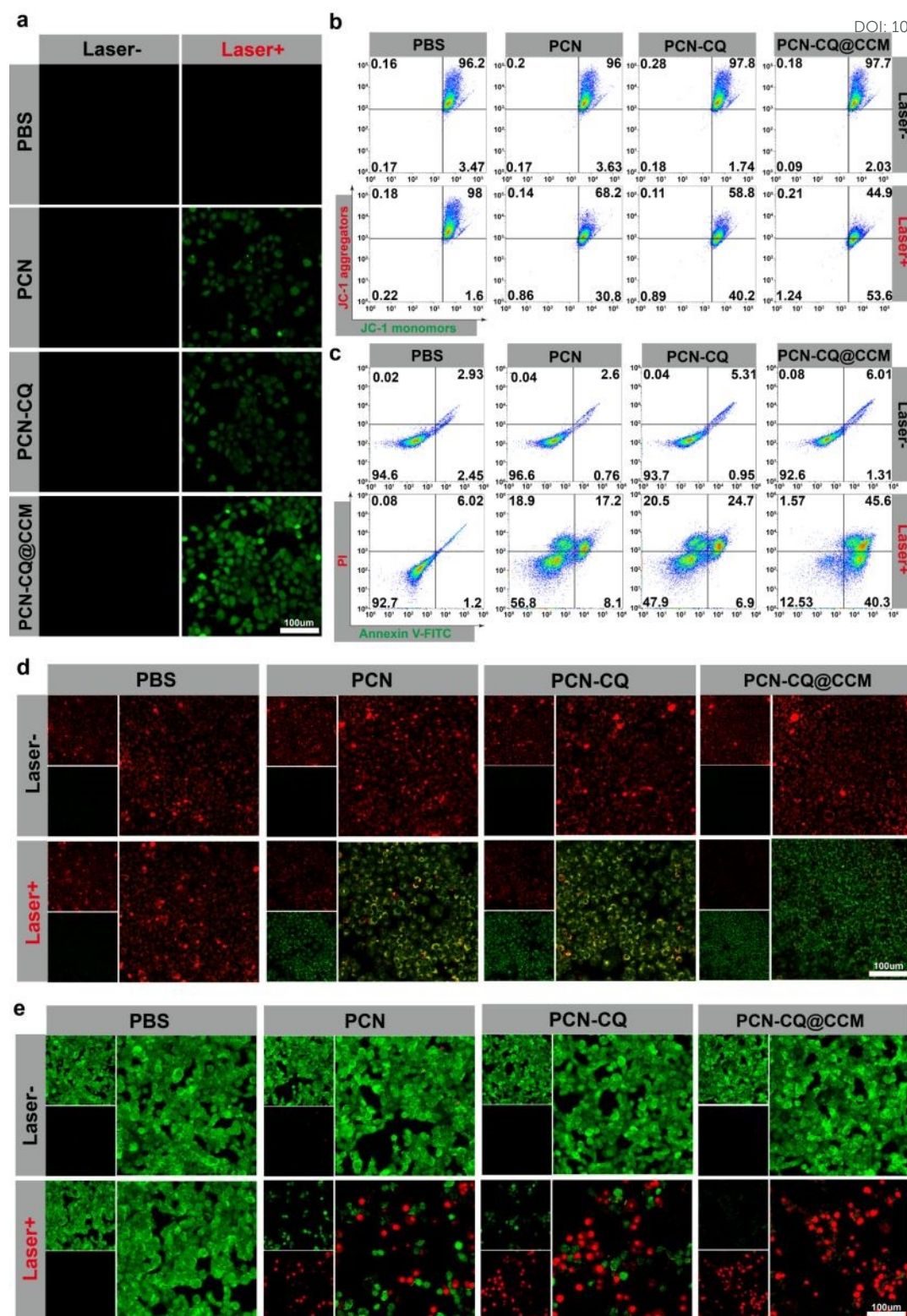
ratio and a lower red fluorescence

Fig. 4 Apoptosis induced by PCN-CQ@CCM. (a) CLSM image of ROS generation in Cal-27 cells after not

receiving or receiving laser, scale bar = 100 μm. (b) FCM detection of the depolarization of mitochondria of Cal-

27 cells after not receiving or receiving laser. (c) FCM detection of the apoptosis/necrosis of Cal-27 cells after not

receiving or receiving laser. (d) CLSM image of mitochondrial depolarization of Cal-27 cells after not receiving or

receiving laser, scale bar = 100 μm. (e) CLSM image of the apoptosis/necrosis of Cal-27 cells after not receiving

or receiving laser, scale bar = 100 μm. (660nm, 100mW/cm^2, 5min)

intensity, indicating that more intracellular mitochondria had undergone membrane potential

depolarization. We hypothesized that more ROS in the cell would lead to more obvious

depolarization of the mitochondrial membrane potential. In addition, FCM was used to

semiquantitatively analyze the depolarization of mitochondrial membrane potential, and similar

results were obtained (Fig. 4b). At the same time, Annexin V-FITC/PI dye was used to detect the

final antitumor performance of PDT in vitro. The CLSM results showed that only the PCN+L,

PCN-CQ+L and PCN-CQ@CCM+L groups showed a red color, representing cell death

fluorescence. The red fluorescence ratio of the PCN-CQ@CCM+L group was higher than those of

the other two groups (Fig. 4e). In addition, using FCM to quantitatively detect cell

necrosis/apoptosis yielded similar results (Fig. 4c). It can be clearly seen that PCN-CQ@CCM,

which has enhanced cell uptake, has a more significant ability to promote apoptosis.

3.4 PCN-CQ@CCM inhibits protective autophagy

However, the autophagy inhibition and apoptosis enhancement effects induced by CQ were not

clearly reflected in the aforementioned experiments. According to previous research on tumor

treatment, traditional treatment methods such as chemotherapy, hyperthermia, and reactive oxygen

stress can induce protective autophagy in tumor cells, and the upregulation of protective

autophagy flow can be used as a resistance mechanism to weaken antitumor therapy. An

increasing number of studies believe that therapeutic strategies targeting the autophagy pathway

are expected to solve the tolerance of tumor treatment. Therefore, we studied the autophagy

performance of PCN-CQ@CCM in the treatment of the Cal-27 tumor cell line. Western blot and

TEM methods are recognized as reliable methods for detecting autophagy. First, we used western

blotting to verify the expression of key proteins in the process of autophagy. Compared with the

PBS+L group, the PCN+L group had a slight upregulation of LC3-Ⅰ and LC3-Ⅱ, indicating that

the higher autophagic flux caused by PDT was triggered. More importantly, the PCN-CQ+L and
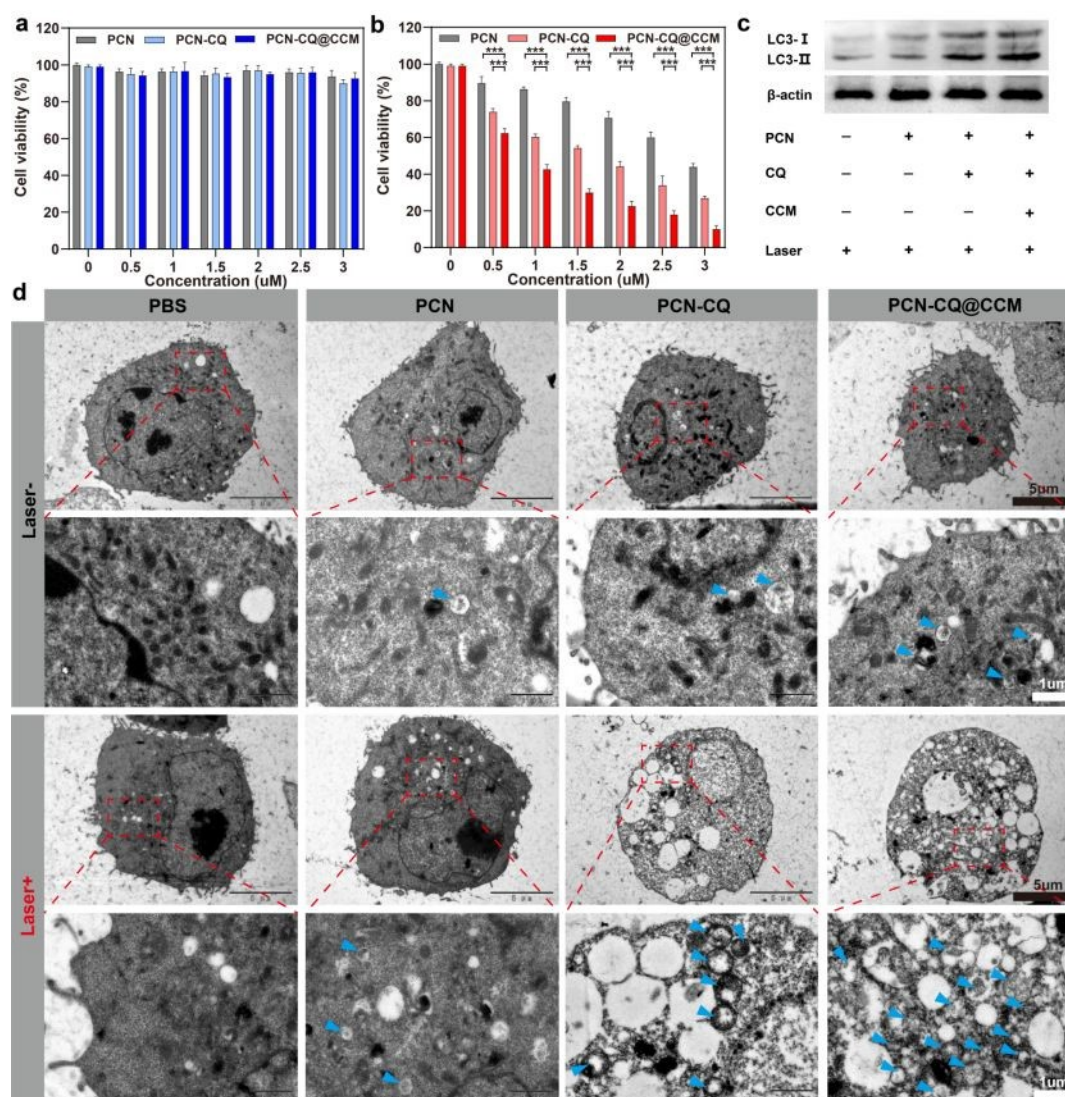

Fig. 5 PCN-CQ@CCM inhibits intracellular protective autophagy. (a) Cal-27 cell viability under dark conditions

after treatment with different concentrations. (b) Cal-27 cell viability under light conditions after treatment with

different concentrations, ***p < 0.001. (c) Bio-TEM image of autophagosomes in cells not receiving or receiving

laser, black scale bar = 5 µm, white scale bar = 1 µm.

PCN-CQ@CCM groups showed significant increases in LC3-II after treatment, which indicated

that CQ released after PDT inhibited the fusion of autophagosomes and lysosomes, preventing the

formation and degradation of autolysosomes, leading to the accumulation of LC3-Ⅱ in the

autophagy stream and playing a role in inhibiting protective autophagy (Fig. 5c). Furthermore, we

used biological TEM to demonstrate this process. Similar to the western blot results, more

autophagosomes were observed in the PCN-CQ+L and PCN-CQ@CCM +L groups than in the

other groups (Fig. 5d). Additionally, the released CQ prevented the formation and degradation of

autolysosomes, leading to the accumulation of autophagy substrates and confirming the successful

inhibition of protective autophagy. Finally, we used the CCK-8 method to evaluate the safety and

phototoxicity of nanomaterials. The results showed that the materials had good biosafety within

the effective concentration of TCPP of 3 µM (Fig. 5a, Fig. S8), and after the cells were exposed to

laser, the activity decreased with the concentration of the material; the antitumor performance of

PCN-CQ@CCM>PCN-CQ>PCN appeared at the same concentration (Fig 5b). Because the

detection of cell viability by the CCK-8 method requires 24 hours after laser treatment, we believe

that the process of autophagy inhibition exerted a further antitumor effect in the subsequent stages

of the experiment.

3.5 PCN-CQ@CCM in vivo diagnosis and treatment

Based on the combined mechanism and excellent effects of PCN-CQ@CCM in vitro treatment,

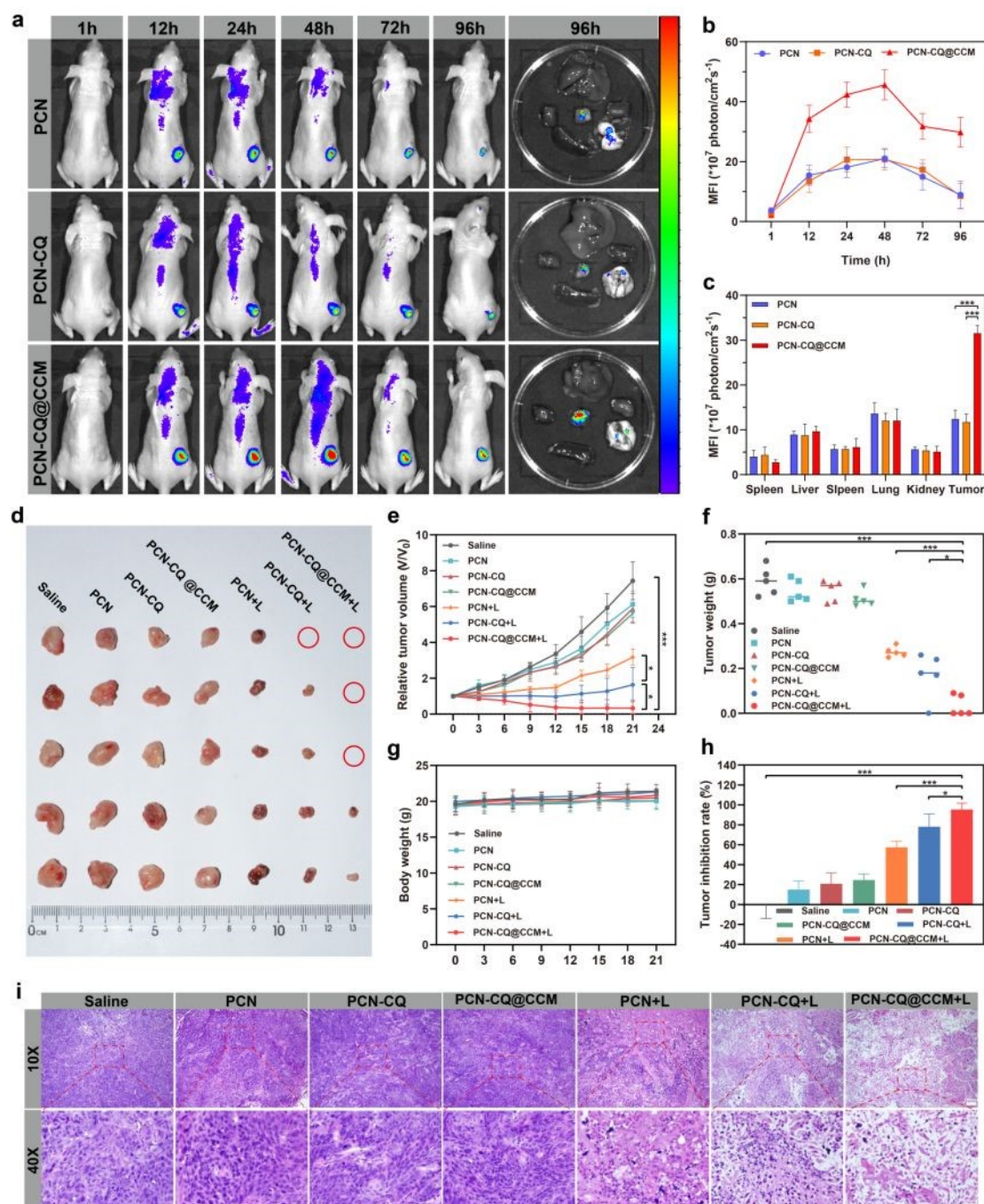we further explored the in vivo diagnosis and treatment effect of PCN-CQ@CCM in oral

Fig. 6 Antitumor capacity of PCN-CQ@CCM in vivo. (a) Animal fluorescence imaging of tumor-bearing nude

mice over time. (b) Quantitative distribution determined by the averaged fluorescence intensity of the tumor over

time. (c) Quantitative distribution determined by the averaged fluorescence intensity of each organ and tumor,

***$p < 0.001$. (d) Digital photos of isolated tumors after the treatment cycle. (e) Tumor volume change curve

during the treatment cycle, *p < 0.05, ***p < 0.001. (f) Isolated tumor weights after the treatment cycle, *p < 0.05,

***p < 0.001. (g) Body weight change curve of tumor-bearing nude mice during the treatment cycle. (h) The final

tumor inhibition rate of each experimental group, *p < 0.05, ***p < 0.001. (i) H&E-stained tissue sections of

tumors after the treatment cycle, above scale bar = 100 μm, below scale bar = 25 μm.

squamous cell carcinoma Cal-27 tumor-bearing nude mice. According to reports, PCN-224 can be

used as an excellent nano-optical probe based on its fluorescence performance, which can be

enriched in solid tumors by passive transportation to play a role in fluorescence diagnosis[36].

However, this passive accumulation method that relies on the EPR effect is restricted by material

properties, tumor types, and anatomical factors and cannot efficiently and accurately achieve

effective enrichment of solid tumor areas, causing the fluorescence diagnosis and even the final

treatment effect based on this to be greatly reduced. The development of biomimetic membrane

technology provides new targeted ideas for the tumor treatment of nanomaterials. Through free

target tumor cell membrane coating, the immune escape of nanomaterials in the circulatory system

and homologous enrichment in the final tumor area can be achieved. This simple targeted

modification technology further enhances the tumor diagnosis and treatment effect of

photodynamic nanomaterials. As shown in (Fig. 6a, b, c), we observed the fluorescence imaging

results of tumor-bearing nude mice after injection of PCN, PCN-CQ and PCN-CQ@CCM via the

tail vein at different time points. With increasing time after injection, the fluorescence intensity of

the tumor site gradually increased, reaching a peak at 24 to 48 h. The fluorescence intensity of the

tumor area of the PCN-CQ@CCM group was significantly higher than that of the control group.

After the final execution of the tumor-bearing nude mice, the PCN-CQ@CCM group tumors had

significantly stronger fluorescence intensity, and the remaining internal organs displayed no obvious fluorescence, suggesting that PCN-CQ@CCM had an excellent targeting enrichment effect. Then, we performed treatments on Cal-27 tumor-bearing nude mice. Tumor-bearing nude mice in each experimental group were administered 1 mg/ml and 200 µl of each injection of nanomaterials via the tail vein, and the tumor-bearing mice in each experimental group were given no laser or laser (660 nm, 100 mW/cm^2, 5 min) processing. Then, we observed the tumor growth periodically and recorded the tumor volume and the weight of the nude mice every three days. All experimental animals were killed after 21 days, and we collected the isolated tumors of each experimental group and took pictures (Fig. 6d). The experimental groups after irradiation had significantly smaller isolated tumors than the nonirradiated experimental groups. Among them, the PCN-CQ@CCM+L group showed that more than half of the tumor was ablated, indicating the best tumor suppression effect. After fixing, sectioning, and staining, the tumor slices of each experimental group were observed with a fluorescence microscope, and the PCN-CQ@CCM+L group slices showed the largest area of cell death under the visual field (Fig. 6i). According to the statistics of tumor volume changes during the treatment cycle (Fig. 6e), compared with the control group and the nonilluminated group, the PCN+L group had a certain tumor growth inhibitory effect during the cycle. The PCN-CQ+L group had a good inhibitory effect in the first half of the cycle, but there was a trend of recurring growth after 18 days, while the PCN-CQ@CCM+L group continued to maintain the trend of tumor ablation and growth inhibition after exposure to laser and showed optimal tumor growth inhibition within 21 days. Statistics on the weight of isolated tumors showed consistent results, and the weight of tumors in the PCN-CQ@CCM+L group was significantly lower than those of other controls (Fig. 6f). According to the statistical calculation of

the tumor cycle growth data, the PCN-CQ@CCM+L group achieved a nearly 100% inhibitory effect, which was significantly higher than the other groups (Fig. 6h). In addition, the weight change of the nude mice during the cycle showed that there was no significant weight fluctuation in each experimental group (Fig. 6g). At the same time, H&E-stained sections of the important organs in vitro were observed with a fluorescence microscope, and the important organs of the nude mice in each experimental group were determined not to be abnormal, confirming that PCN-CQ@CCM had excellent biological safety and caused no obvious damage to nontumor tissues (Fig. S9). In addition, the rabbit hemolysis experiment proved that the PCN-CQ@CCM material has good blood circulation safety (Fig. S10).

4. Conclusion

In this work, we synthesized a biomimetic nanodelivery platform camouflaged by oral cancer cell membranes through a simple method and realized the precise targeted treatment of tumors with PDT and an autophagy inhibition strategy. The results showed that our synthesized biomimetic nanoplatform PCN-CQ@CCM had uniform, good morphology and particle size, specific selectivity for homologous Cal-27 cells and immune escape for mononuclear macrophages. The excellent homologous enrichment ability enhanced the uptake of nanoparticles in the tumor area, and the enhanced fluorescence signal improved the tumor diagnosis ability. The active targeting strategy enhanced the induced ROS damage ability of the nanoplatform while accurately inhibiting the anti-damage repair mechanism of protective autophagy and achieved a nearly 100% inhibition rate of oral squamous cell carcinoma in 21 days with a single dose. This noninvasive and time-space controllable nanodiagnosis and treatment model has excellent antitumor and

functional tissue preservation functions. It is expected to replace conventional comprehensive treatment of oral cancer and to broaden new horizons for the precise treatment of oral cancer.

Conflicts of interest

The authors declare no competing financial interest.

Acknowledgements

All animal procedures were performed in accordance with the Guidelines for Care and Use of Laboratory Animals of Peking University and approved by the Animal Ethics Committee of Biomedical Ethics Committee of Peking University.

References

[1] Mody MD, Rocco JW, Yom SS, Haddad RI, Saba NF, *Lancet*, 2021, **S0140-6736**(21), 01550-6.

[2] Chinn SB, Myers JN, *J Clin Oncol*, 2015, **33**(29), 3269-3276.

[3] Inhestern J, Schmalenberg H, Dietz A, Rotter N, Maschmeyer G, Jungehülsing M, Grosse-Thie C, Kuhnt T, Görner M, Sudhoff H, Wittekindt C, Guntinas-Lichius O, *Ann Oncol*, 2017, **28**(8), 1917-1922.

[4] Leeman JE, Li JG, Pei X, Venigalla P, Zumsteg ZS, Katsoulakis E, Lupovitch E, McBride SM, Tsai CJ, Boyle JO, Roman BR, Morris LGT, Dunn LA, Sherman EJ, Lee NY, Riaz N, *JAMA Oncol*, 2017, **3**(11), 1487-1494.

[5] Kuriakose MA, *Indian J Med Paediatr Oncol*, 2015, **36**(3), 137-9.

[6] Su J, Lu S, Jiang S, Li B, Liu B, Sun Q, Li J, Wang F, Wei Y, *Adv Mater*, 2021, **33**(21), e2100619.

[7] Pham TC, Nguyen VN, Choi Y, Lee S, Yoon J, *Chem Rev*, 2021, **28**.

[8] Xue X, Huang Y, Bo R, Jia B, Wu H, Yuan Y, Wang Z, Ma Z, Jing D, Xu X, Yu W, Lin TY, Li Y, *Nat Commun*, 2018, **9**(1), 3653.

[9] Huang X, Deng G, Han Y, Yang G, Zou R, Zhang Z, Sun S, Hu J, *Adv Sci (Weinh)*, 2019, **6**(20), 1901461.

[10] Wu W, Shi L, Duan Y, Xu S, Shen L, Zhu T, Hou L, Meng X, Liu B, *Biomaterials*, 2021, **274**, 120870.

[11] Lucky SS, Soo KC, Zhang Y, *Chem Rev*, 2015, **115**(4), 1990-2042.

[12] Zhou Z, Song J, Nie L, Chen X, *Chem Soc Rev*, 2016, **45**(23), 6597–6626.

[13] Felsher, D. W, *Nat. Rev. Cancer*, 2003, **3**, 375−380.

[14] Abbas M, Zou Q, Li S, Yan X, *Adv Mater*, 2017, **29**(12).

[15] Wang D, Wu H, Lim WQ, *Adv Mater*, 2019, **31**(27), e1901893.

[16] Wang Z, Liu B, Sun Q, Feng L, He F, Yang P, Gai S, Quan Z, Lin J, *ACS Nano*, 2021, **23**.

[17] Cai Z, Xin F, Wei Z, Wu M, Lin X, Du X, Chen G, Zhang D, Zhang Z, Liu X, Yao C, *Adv Healthc Mater*, 2020, **9**(1), e1900996

[18] Zhang L, Cheng Q, Li C, Zeng X, Zhang XZ, *Biomaterials*, 2020, **248**, 120029.

[19] Liu Z, Hurst DR, Qu X, Lu LG, Wu CZ, Li YY, Li Y, *Mil Med Res*, 2020, 7(1), 48.

[20] Peña-Oyarzún D, Reyes M, Hernández-Cáceres MP, Kretschmar C, Morselli E, Ramirez-Sarmiento CA, Lavandero S, Torres VA, Criollo A, *Front Oncol*. 2020, 10, 602661.

[21] Khan T, Relitti N, Brindisi M, Magnano S, Zisterer D, Gemma S, Butini S, Campiani G, *Med Res Rev*, 2020, 40(3), 1002-1060.

[22] Chen M, Yang D, Sun Y, Liu T, Wang W, Fu J, Wang Q, Bai X, Quan G, Pan X, Wu C, *ACS Nano*, 2021, **15**(2), 3387-3401.

[23] Ma Y , Chen H , Hao B , Zhou J , He G , Miao Z , Xu Y , Gao L , Zhou W , Zha Z, *J Mater Chem B*, 2018, 6(37), 5854-5859.

[24] Yang B, Ding L, Yao H, Chen Y, Shi J, *Adv Mater*, 2020, **32**(12), e1907152.

[25] Izci M, Maksoudian C, Manshian BB, Soenen SJ, *Chem Rev*, 2021, **121**(3), 1746-1803.

[26] Xie Y, Jiang J, Tang Q, Zou H, Zhao X, Liu H, Ma D, Cai C, Zhou Y, Chen X, Pu J, Liu P, *Adv Sci (Weinh)*, 2020, **7**(16), 1903323.

[27] Liu Z, Zou H, Zhao Z, *ACS Nano*, 2019, **13**(10), 11283–11293.

[28] Li Y, Tang J, He L, Liu Y, Liu Y, Chen C, Tang Z, *Adv Mater*, 2015, **27**(27), 4075-80.

[29] Ishida T, Ichihara M, Wang X, Yamamoto K, Kimura J, Majima E, Kiwada H, *J Control Release*, 2006, **112**(1), 15-25.

[30] Gao W, Hu CM, Fang RH, Luk BT, Su J, Zhang L, *Adv Mater*, 2013, 25(26), 3549-53.

[31] Fang RH, Kroll AV, Gao W, Zhang L, *Adv Mater*, 2018, **30**(23), e1706759.

[32] Li SY, Cheng H, Xie BR, Qiu WX, Zeng JY, Li CX, Wan SS, Zhang L, Liu WL, Zhang XZ, *ACS Nano*, 2017, **11**(7), 7006-7018.

[33] Li SY, Cheng H, Qiu WX, Zhang L, Wan SS, Zeng JY, Zhang XZ, *Biomaterials*, 2017, **142**, 149-161.

[34] Park J, Jiang Q, Feng D, Mao L, Zhou HC. *J Am Chem Soc*, 2016, **138**(10), 3518–3525

[35] Feng Q, Yang X, Hao Y, Wang N, Feng X, Hou L, Zhang Z. *ACS Appl Mater Interfaces.* 2019, **11**(36), 32729-32738.

[36] Wang Z, Liu B, Sun Q, Dong S, Kuang Y, Dong Y, He F, Gai S, Yang P, *ACS Appl Mater Interfaces*. 202, **12**(15), 17254-17267.